The Astrophysical Journal, 727:121 (11pp), 2011 February 1 doi:10.1088/0004-637X/727/2/121

PITCH-ANGLE DISTRIBUTIONS AND TEMPORAL VARIATIONS OF 0.3–300 keV SOLAR IMPULSIVE ELECTRON EVENTS

L. Wang[1], R. P. Lin[1,2,3], and Säm Krucker[1]
[1] Space Sciences Laboratory, University of California, Berkeley, CA 94720-7450, USA; wanglh@berkeley.edu
[2] Department of Physics, University of California, Berkeley, CA 94720-7300, USA
[3] School of Space Research, Kyung Hee University, Yongin, Gyeonggi, Republic of Korea
Received 2010 June 26; accepted 2010 November 22; published 2011 January 12

ABSTRACT

We investigate the propagation of ∼0.3–300 keV electrons in five solar impulsive electron events, observed by the *WIND* three-dimensional Plasma and Energetic Particle instrument, that have rapid-rise and rapid-decay temporal profiles. In two events, the temporal profiles above 25 keV show a second peak of inward-traveling electrons tens of minutes after the first peak, followed by a third peak due to outward-traveling electrons minutes later—likely due to reflection/scattering first at ∼0.7–1.7 AU past the Earth, and then in the inner heliosphere inside 1 AU. In the five events, below a transition energy E_0 (∼10–40 keV), the pitch-angle distributions are highly anisotropic with a pitch-angle width at half-maximum (PAHM) of $<15^\circ$ (unresolved) through the time of the peak; the ratio Λ of the peak flux of scattered ($22.^\circ5$–90° relative to the outward direction) to field-aligned scatter-free (0°–$22.^\circ5$) electrons is $\lesssim$0.1. Above E_0, the PAHM at the flux peak increases with energy up to 85° at 300 keV, and Λ also increases with energy up to ∼0.8 at 300 keV. Thus, low-energy electrons propagated essentially scatter-free through the interplanetary medium, while high-energy electrons experienced pitch-angle scattering, with scattering strength increasing with energy. The transition energy E_0 between the two populations is always such that the electron gyroradius (ρ_e) is approximately equal to the local thermal proton gyroradius (ρ_{Tp}), suggesting that the higher energy electrons were scattered by resonance with turbulent fluctuations at scale $\gtrsim\rho_{Tp}$ in the solar wind.

Key words: Sun: particle emission

Online-only material: color figures

1. INTRODUCTION

Solar impulsive electron events were first observed at energies above ∼40 keV (Van Allen & Krimings 1965; Anderson & Lin 1966), with fast-rise, slow-decay temporal profiles indicative of significant scattering in the interplanetary medium (IPM). Later, events were detected down to keV energies (and even to ∼0.1 keV; Gosling et al. 2003), occasionally with fast-rise, fast-decay profiles that imply essentially scatter-free propagation in the IPM (Lin 1974). Near solar maximum, $\gtrsim10^2$ events month^{-1} on average occur over the whole Sun (see Lin 1985, for review), making these the most common impulsive solar particle acceleration phenomenon observed in the IPM. They are often accompanied by low energy, ∼MeV/nucleon ion emissions that are highly enriched in ^{3}He and heavy ions with high charge states (e.g., Fe^{20+}; see Reames 1999 for review). These electron/^{3}He-rich events form the class of "impulsive"solar energetic particle (SEP) events, so-called because the associated soft X-ray burst (when present) is of short duration. The well-known large SEP events that have been observed since the first ground level detection (Forbush 1946) belong to a second class, the so-called Gradual SEP events (with long duration associated soft X-ray burst). These occur on average ∼once per month near solar maximum, and they are characterized by intense proton fluxes, small electron/proton ratios, and normal coronal abundances and charge states. Reames (1995, 1999) and references therein suggested that impulsive SEP events are produced in impulsive flares at the Sun (although the majority of these events do not have an associated flare (L. Wang et al. 2010, in preparation)), whereas gradual SEP events arise from acceleration by shocks driven by fast coronal mass injections.

For solar impulsive electron events, Krucker et al. (1999) found that the injection of the >25 keV electrons at the Sun were often delayed by ∼10 to ∼30 minutes after the type III radio bursts, and Haggerty & Roelof (2002) reported a median delay of ∼10 minutes for 38–315 keV electrons. Wang et al. (2006) showed that the flux versus time injection profiles at the Sun for three strongly scatter-free electron events observed down to ∼0.4 keV fit well to isosceles triangles (equal rise and fall times), and that the ∼13–300 keV electrons were injected starting 7.6 ± 1.3 minutes after the type III bursts but the ∼0.4–10 keV electrons were injected beginning 9.1 ± 4.7 minutes before the type III bursts, indicating that the ∼0.4–10 keV electrons generate the radio emission (consistent with type III radio emissions and parent Langmuir waves observed in situ simultaneously with the arrival of ∼2–10 keV electrons at 1 AU (e.g., Ergun et al. 1998)). Cane & Erickson (2003) and Cane (2003) argued from radio observations, however, that the delays of high-energy electrons were due to propagation effects in the IPM. In this study, we will use in situ electron observations to examine the propagation of different energy electrons in the IPM for solar impulsive electron events.

As energetic electrons propagate outward from the Sun along diverging interplanetary magnetic field (IMF) lines, we expect that adiabatic motion (the invariance of $\sin^2\alpha/B$) would focus them to small pitch angle (PA), α, but nonadiabatic wave-particle interactions can scatter them to large PA (pitch-angle scattering/diffusion). Thus, in situ observations of electron pitch-angle distributions (PADs) provide important information on local electron–wave interactions, while the flux versus time profiles integrate the effects of injection and propagation from the Sun to Earth. Using ISEE-3 electron observations of ∼2 keV to

1 MeV, Potter et al. (1980) and Lin et al. (1981) reported that the PAHM (PA width at half-maximum) of PADs was <13° for electrons below ~10 keV and >30°–40° above 15 keV. Using *ACE*/SWEPAM electron observations at lower energies, ~73 eV to ~1.4 keV, Gosling et al. (2003) reported that the PAHM of solar electron events was ~60° at ~370 eV. de Koning et al. (2006, 2007) also reported that in solar electron events detected at 73–1370 eV by *ACE*/SWEPAM, the beam angular width varied with energy from ~15° to >75°.

With *WIND* three-dimensional (3D) electron observations from solar wind plasma to >300 keV, we analyze the temporal behavior and the PADs for five solar impulsive electron events that have short time durations, low pre-event background and good count statistics. We illustrate the characteristics of these events with detailed observations of one representative event on 2002 October 20 in Section 2, and briefly describe the other four events in the Appendix. In Section 3, we summarize and discuss the results of all five events.

2. OBSERVATIONS AND DATA ANALYSIS

The *WIND* 3D Plasma and Energetic Particle instrument (3DP) provides full 3D measurements of electron distributions from solar wind thermal plasma to ~400 keV (Lin et al. 1995). Silicon semiconductor telescopes (SSTs) measure ~20–400 keV electrons with energy resolution of ~7 keV FWHM and $\Delta E/E \approx 0.3$ and angular resolution of $22.^{\circ}5 \times 36^{\circ}$, while electron electrostatic analyzers (EESA-L and EESA-H) measure ~3 eV to 30 keV electrons with $\Delta E/E \approx 0.2$ and angular resolution of $22.^{\circ}5 \times 22.^{\circ}5$. The flux in each 3D angular bin is assigned a PA calculated for the center of the angular bin using the vector IMF direction measured by the *WIND* MFI instrument (Lepping et al. 1995). Then the 3D data are sorted into eight PA bins with a $22.^{\circ}5$ angular resolution, with some overlap between adjacent bins. If the IMF points sunward (anti-sunward), then the four $22.^{\circ}5$ PA bins from 90° to 180° cover electrons traveling outward from (toward) the Sun and the other four bins from 0° to 90° cover inward-traveling (outward-traveling) electrons.

We select five solar impulsive electron events (listed in Table 1) with short time durations, strongly scatter-free flux-time profiles, low pre-event background, and good count statistics observed by *WIND*/3DP from ~0.3 to ~300 keV. During the five events, the *WIND* spacecraft was located in the solar wind, without magnetic connection to the Earth's bow shock. Also, for the SSTs, we correct for the ~15% of incident electrons that scatter out of the silicon detector (~85% stop in the detector and deposit all their energy, E_{in}) and leave only a fraction of E_{in}, producing a spectrum that is approximately evenly distributed in energy below E_{in} (Berger et al. 1969). In this section, we illustrate the characteristics of these events with detailed observations of one representative event on 2002 October 20.

2.1. Flux Versus Time

The 2002 October 20 impulsive electron event was clearly detected down to ~0.26 keV and up to $\gtrsim$310 keV. The left panel of Figure 1 shows the outward-traveling electron fluxes (averaged over 90°–180° PA since the IMF pointed sunward) versus time at energies from ~0.2 to 310 keV. Figure 2 shows electron fluxes versus time in four outward and four inward PA bins at 66 keV (left) and 4.2 keV (right), after subtracting pre-event electron background and instrumental background.

Table 1
Five Solar Impulsive Electron Event Properties

Date	V_{SW} (km s^{-1})	L_{parker} (AU)	kT_p [a] (eV)	$E_{\rho_e=\rho_{Tp}}$ [b] (keV)	E_0 [c] (keV)
1998 July 11	660	1.06	6.8	12.4	~15
1998 August 29	390	1.16	11.5	20.8	~10
2001 July 18	550	1.09	33.4	57.9	~40
2002 October 20	670	1.06	26.6	46.7	~30
2002 October 21	610	1.07	22.1	39.1	~30

Notes.
[a] Parker spiral field length from the Sun to 1 AU.
[b] The energy of electrons with $\rho_e = \rho_{Tp}$.
[c] The transition energy between low-energy (nearly scatter-free) and high-energy (scattered) electron populations.

At 66 keV, the flux-time profiles at 1 AU exhibit three peaks, 1 at ~1437UT, 2 at ~1610UT, and 3 at ~1640UT. At 4.2 keV, only peaks 1 and 2, respectively, at ~1550UT and ~2120UT, are clearly evident above background. An abrupt flux increase occurred during 1525–1535UT simultaneously in all inward PA bins (also evident in outward PA bins with low fluxes) at all energies from 27 to 310 keV, coincident with the sudden rotation of the IMF to a strongly northward direction (bottom panels of Figure 2), suggesting a change in magnetic connection to the Sun and/or to the heliosphere beyond 1 AU.

2.1.1. Peak 1

Peak 1, detected from ~0.26 to 310 keV, is due to the initial passage of outward-traveling electrons at the spacecraft. The flux-time profiles at all energies exhibit a nearly symmetric rapid-rise, rapid-decay peak, followed by a slow decay (not seen below ~1 keV) at flux levels much lower than the peak (left panel of Figure 1). Velocity dispersion is clearly evident from ~0.3 to 310 keV. For electrons above ~25 keV, the times, t_i, of the peak fluxes at different velocities, V_i, fit well to a straight line (see the bottom of the left panel of Figure 3), $L = V_i[t_i - t_0]$, implying a simultaneous solar injection at these energies with the peak time $t_{01} = 1412 \pm 0002$UT followed by travel along the same path of length $L_1 = 1.25 \pm 0.10$ AU. For electrons below 15 keV, the linear fit to the peak-flux times gives a path length estimate of $L_{1b} = 1.16 \pm 0.08$ AU (see the right panel of Figure 3) and a release peak time of $t_{01b} = 1422 \pm 0006$UT. The two lengths are consistent with each other within errors, and are slightly larger than the smooth spiral field length of 1.06 AU calculated for the observed solar wind speed V_{SW} of 660 km s^{-1} (Table 1). Such profiles and velocity dispersion imply that most of the outward-traveling electrons (those in peak 1) propagated through the IPM with little or no backscattering (mean free path >1 AU), since significant backscattering (mean free path $\lesssim$0.4 AU) through the IPM would produce an asymmetric peak with a strong, very slow decay (Lin 1974) and a much larger path length.

For the outward-traveling electrons in peak 1, we obtain the injection profiles at the Sun from forward fitting to the flux-time profiles observed at 1 AU, by assuming triangular injections with equal rise and fall times, and taking into account the energy channel width and assuming scatter-free propagation along a 1.2 AU path through the IPM (see Wang et al. 2006 for details of triangular fitting). The left panels of Figure 4 show that the fits (red curves) are very good through the rapid-rise, rapid-fall phase. Afterward, the observed electrons fluxes (black curves) show a very weak (<2% of the peak flux)

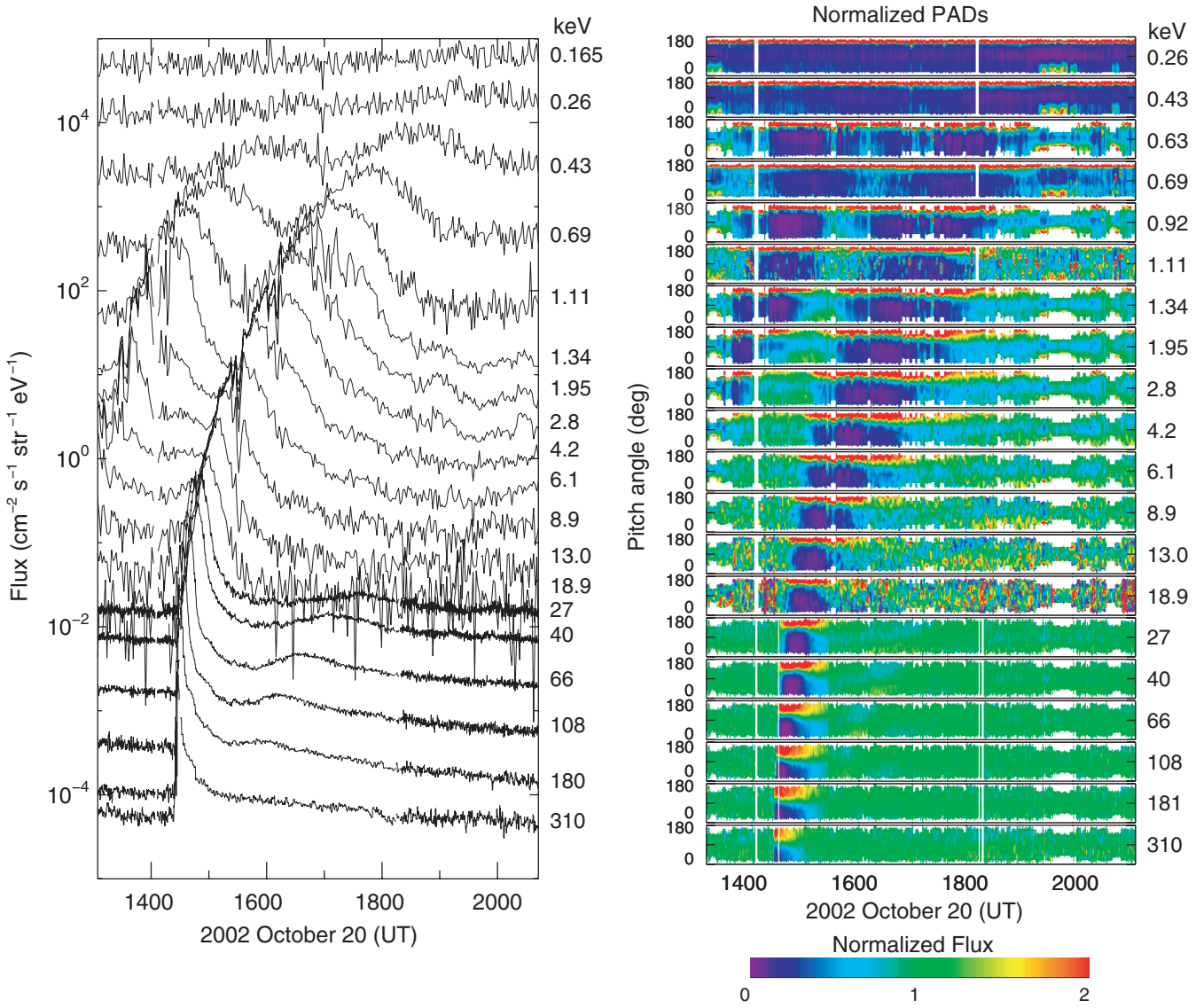

Figure 1. Overview plot for the 2002 October 20 event. Another impulsive electron event occurred a few hours earlier with less count statistics. The IMF was pointing toward the Sun. The left panel shows the flux of electrons traveling anti-parallel (outward) to the IMF observed by EESA-L (0.17–1.11 keV; 96 s average), EESA-H (1.34–18.9 keV; 96 s average), and SST (27–310 keV; 12 s average). The right panels show electron PADs normalized by the PA averaged flux for each time bin and energy channel. Isotropic distributions show normalized values around 1 (green) in all PA directions, while beamed distributions have larger values (red) in the beaming direction and lower values (indigo) in other directions. The labeled energy is the center energy for each channel.

(A color version of this figure is available in the online journal.)

slow-decay tail at energies above ∼2 keV. The inferred triangular injection profiles at 0.4–310 keV are shown in the right panel of Figure 4. This event has three possible associated type III radio bursts measured at ∼14 MHz by *WIND*/WAVES. On average, electron injections above ∼13 keV start 14.3 ± 1.6 minutes after the coronal release of the first type III radio burst and last for ∼20 minutes, while electron injections below ∼6–9 keV begin 20.0 ± 6.9 minutes earlier than the first type III burst and last for ∼110 minutes.

2.1.2. Peak 2

At 66 keV (left panels of Figure 2), the flux-time profiles of inward-traveling electrons show a broad, nearly symmetric peak (No. 2) around 1610UT in the inward PA bins, with the maximum that is ∼1%–10% of peak 1 at 1437UT in the outward PA bins. This symmetric inward peak was clearly detected at 27–180 keV, with a velocity dispersion giving an injection peak time $t_{02} = 1430 \pm 0017$UT and a path length $L_2 = 4.74 \pm 0.81$ AU (middle of the left panel of Figure 3). It suggests that these inward-traveling electrons originated beyond the spacecraft, likely from magnetic mirroring/scattering of outward-traveling electrons by an abrupt boundary at the heliocentric distance of ∼2 AU (since $L_2 - L_1 \approx 3.5$ AU, about two times the smooth spiral field length between the Earth and the 2.2 AU heliocentric distance), whereas across-90°-PA scattering spread out over a long path would favor an asymmetric slow-rise, very slow-delay profile. Peak 2 was poorly detected below 25 keV by EESA-H due to the low signal-to-noise ratio (see the right panels of Figure 2, for example).

2.1.3. Peak 3

At 1 AU, the in situ flux-time profiles of outward-traveling electrons exhibit a rough symmetric peak (No. 3) at 27–180 keV, superimposed on the slow decay of peak 1 (the left panel of

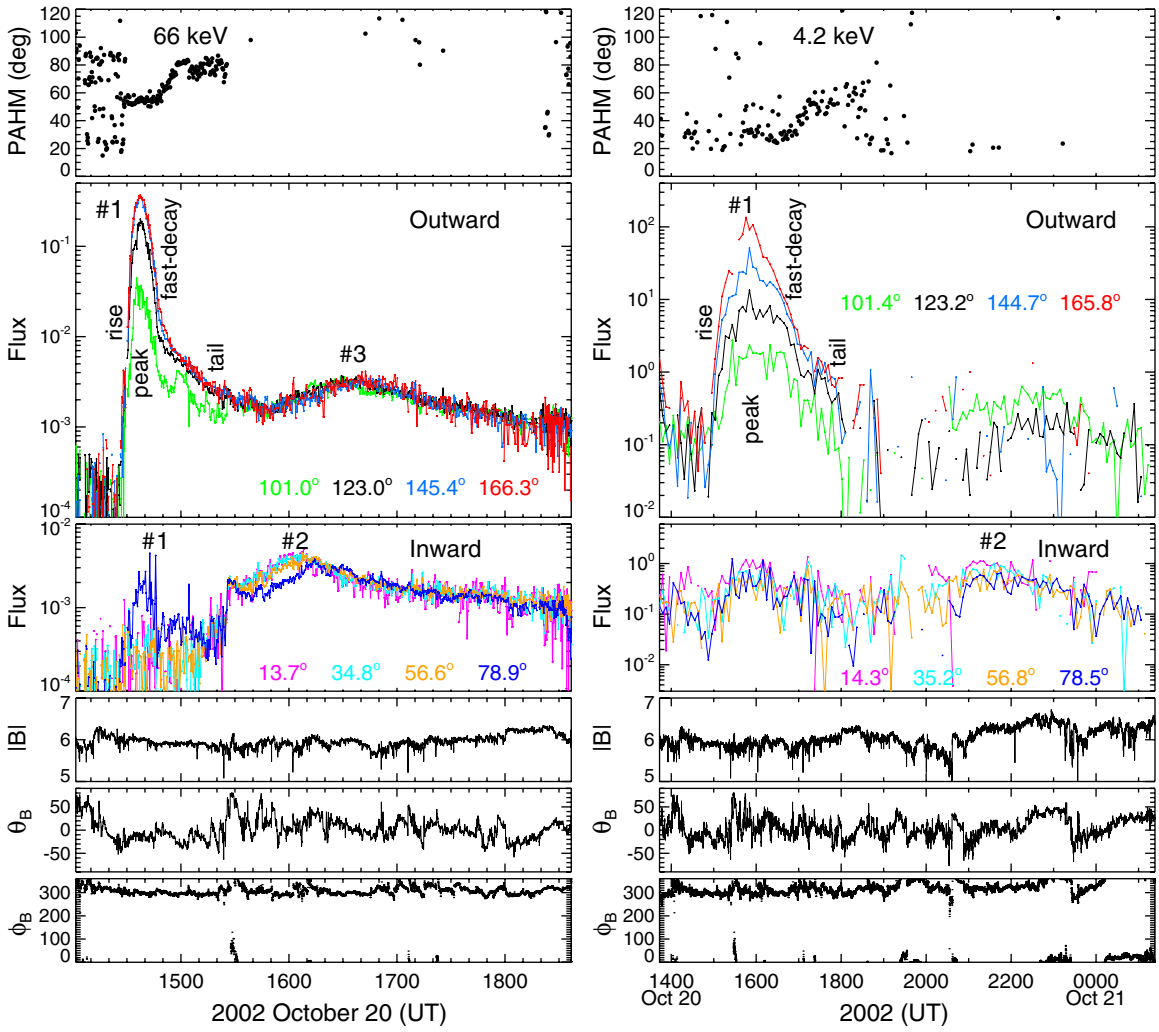

Figure 2. Temporal profiles of background-subtracted electron fluxes at 66 keV (left) and 4.2 keV (right) in four outward-traveling (101°, 123°, 145°, 166°; bin average angles) and four inward-traveling (14°, 35°, 57°, 79°) PA bins for the 2002 October 20 event. Colored curves indicate the 12 s (5 minute) average flux in different PA bins at 66 keV (4.2 keV). The top panel is the temporal profile of the electron PAHM, showing larger fluctuations before and after the event (when the background-subtracted electron fluxes are at noise levels). The bottom panels show the magnitude, polar angle, and azimuthal angle of the IMF measured by *WIND*/MFI.

(A color version of this figure is available in the online journal.)

Figure 3 and the second left panel of Figure 2). The velocity dispersion analysis of those peak-flux times gives an injection peak time $t_{02} = 1438 \pm 0013$UT and a path length $L_3 = 6.25 \pm 0.60$ AU (top of the left panel of Figure 3). We suspect that these outward-traveling electrons mainly originated from reflection of inward-traveling electrons in peak 2 by converging IMF between the Sun and Earth, e.g., at the heliocentric distance of ~0.3 AU estimated from the smooth spiral field model.

2.2. Pitch-angle Distributions

The right panels of Figure 1 show the electron PADs at 0.3–310 keV normalized by the PA averaged flux for each time bin and energy channel. For peak 1, Figure 5 shows six normalized 3D angular distributions from 1.3 to 108 keV measured at time of the peak flux at each energy. At 1.3, 13, and 27 keV, the 3D angular distributions exhibit similar PAHMs of ~30° or less, limited by instrumental resolution. At 40, 66, and 108 keV, however, the distributions clearly broaden with increasing energy. Figure 6 compares the normalized PADs of 1.34 and 108 keV at the peak after background subtraction. At 108 keV, the PAD is ~2.5 times broader (PAHM of 66° versus $\lesssim$26°, as determined from linear interpolation between two bins bracketing the half-value of maximum flux) than at 1.34 keV. Figure 7 shows the typical PAHM as a function of energy at the rise, peak, fast decay, and slow tail for peak 1 of this event in the top right panel.

At low energies, ~0.4–27 keV, the electron PADs are strongly beamed along the IMF (right panels of Figure 1) with PAHM $\lesssim$ 30° on the rise and through the peak (the top right panel of Figures 2 and 7). The maximum flux in the field-aligned PA 22.5 bin is ~3–8 times larger than that in the adjacent PA 22.5 bin (see the second right panel of Figure 2, for example). Simulations of the instrumental angular response show that these ratios correspond to an actual PAHM of <15°, assuming a Gaussian function for the PAD. These highly anisotropic PADs at low energies would be expected when electrons undergo adiabatic focusing along diverging IMF lines with little PA scattering. In the fast decay after the peak, the beamed PADs broaden to ~30°–40° PAHM. This PA broadening is related to later arrivals of electrons with smaller parallel speeds $V_\parallel = V\,|\cos(\alpha)|$ and/or the increasing scattering with time. In the decay phase, although field-aligned ($V_\parallel \sim V$) electrons dominate the flux,

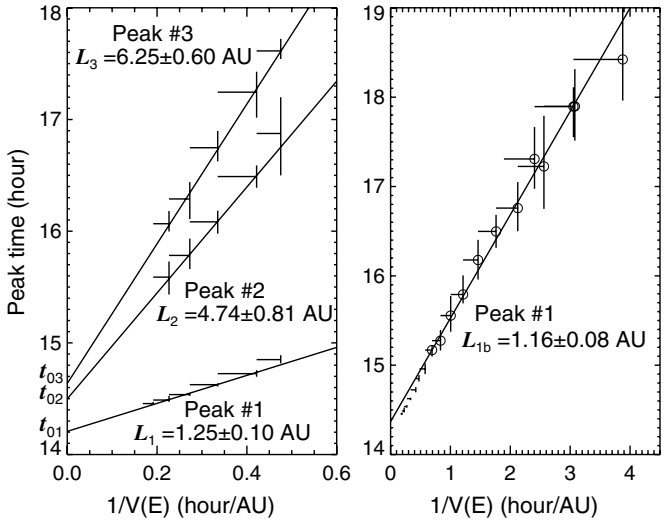

Figure 3. Velocity dispersion analysis of the peak-flux time vs. the inverse speed above 25 keV (left) and below 15 keV (right) for the 2002 October 20 event. For each energy channel, the speed V_i is determined by the lower bound since the flux decreases rapidly with energy due to the hard energy spectrum. The left panel shows the times for peaks 1 (bottom), 2 (middle), and 3 (top) above 25 keV. These times align well on a straight line as a function of the inverse speed, $t_i = t_0 + L/V_i(E)$, giving estimates of the path length L (slope) and the release peak time t_0 (Y-axis intercept). The right panel shows the times for peak 1 above 15 keV and below (circles), with the linear fit to the peak times below 15 keV.

non-field-aligned (smaller $V_\parallel$) electrons show a slower flux decrease (see the second right panel of Figure 2, for example), and then their flux ratio to field-aligned electrons increases with time, leading to the broadening of PADs with time (see the top right panel of Figure 2, for example). The PAHM then reaches typically ∼50°–60° PAHM in the slow tail. Above ∼50°, the simulations show that the PAHM determined by the procedure of Figure 6 would reflect the actual PAHM.

At high energies, ∼30–300 keV, the electron PADs become broader with energy. During the peak, the PAHM increases from ∼42° at 40 keV to ∼80° at 310 keV, but the flux-time profiles keep a strongly "scatter-free"shape. The maximum flux in the field-aligned PA bin becomes similar to the adjacent PA bin. Such PADs and temporal profiles imply that at high energies, outward-traveling electrons experienced strong local PA scattering that would broaden the PA distribution without significantly distorting the temporal profile, and the scattering strength increases with energy. These PADs also broaden with time after onset above 70 keV, as expected for later arrivals of scattered electrons and/or the increasing scattering with time, while below 70 keV the PADs broaden after the fast decay (Figure 2, left). In the slow-decay tail, the PAHM reaches around 65°, 80°, 85°, 87°, and 90°, respectively, at 40, 66, 108, 180, and 310 keV, and stays roughly constant until the start of peak 2 (when present).

2.3. PA Dispersion

If the electrons at the same energy are produced simultaneously at all PAs and then all propagate the same distance l to reach the spacecraft without scattering, then electrons with larger $V_\parallel$ would arrive earlier, i.e., PA dispersion: $t(\alpha) = t_{0'} + l/V_\parallel(\alpha)$. Figure 8 shows that the peak-flux times of the 66 keV electrons at different α linearly fit to a distance l of 0.004 ± 0.05 AU for peak 1 (bottom) and an l of 0.21 ± 0.19 AU for peak 2 (top). This l is a measure of the average travel distance between scatterings near the spacecraft, and indicates a small local mean free path and thus strong local scattering near the spacecraft. Similar results are obtained for all the energies with peaks 1 and 2 clearly detected.

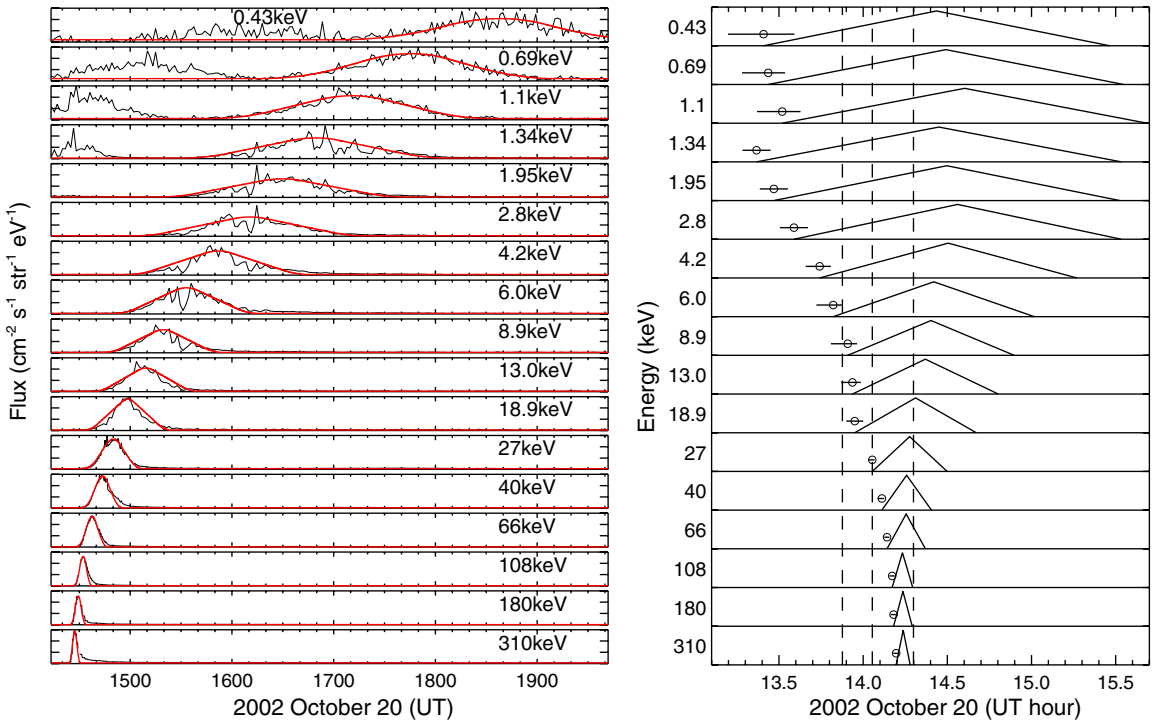

Figure 4. Triangular injection fitting for the 2002 October 20 event at 0.4–310 keV. Left: the red curves are the best fit to the fast rise, fast fall of in situ temporal profiles of electron fluxes at 1 AU (black curves). Right: inferred electron injection profiles at the Sun. The circles indicate the start time of solar electron injections, while the vertical dash lines indicate the solar release of type III radio bursts.

(A color version of this figure is available in the online journal.)

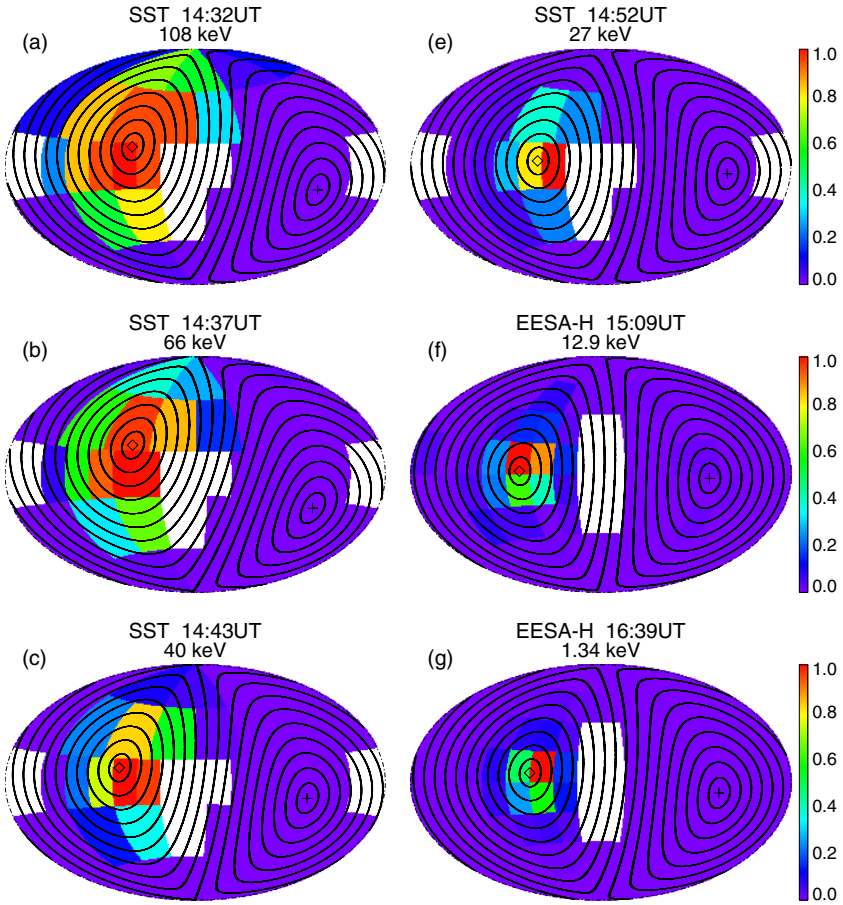

Figure 5. Normalized 3D electron angular distributions measured at the peak of 1.3 and 13 keV (EESA-H) and of 27–108 keV (SST) for the 2002 October 20 event. The SST distributions are averaged over ~24 s and the EESA-H distributions are averaged over ~96 s after removal of the pre-event background. The high-background bins due to solar X-rays have been excluded. The cross (diamond) indicates the direction parallel (anti-parallel) to the IMF. The black curves represent the iso-PA contours at every 10°.

(A color version of this figure is available in the online journal.)

2.4. Local Inward-traveling Electrons

During peak 1, an inward-flux increase was clearly detected at ~66–310 keV (see Figures 2 and 6, for example). It appears only in the 79° PA bin with the maximum slightly delayed from the adjacent outward 101° PA bin, while no significant fluxes show above the background in the other three inward PA bins. The flux ratio of the inward 79° PA bin to the adjacent outward 101° PA bin is 8 outward 101° PA bin is 8%–15% at the peak and increases to 20%–50% during the decay. The overlapping between adjacent PA bins, introduced by the instrumental response, would only account for a flux ratio <5%, based on observations. Thus, the inward flux observed at 66–310 keV was mainly due to inward-traveling electrons, likely caused by local weak, small-angle scattering across 90° PA, or adiabatic mirroring near 90° PA at stronger downstream IMF that was close to the spacecraft. For example, the IMF was 6.3 nT around 1415 UT at the spacecraft (bottom panels of Figure 2), and at the observed V_{SW} of 660 km/s, this field would travel only $\lesssim$0.006 AU beyond at 1437UT when the 66 keV outward-traveling electrons peaked at the spacecraft with an IMF of ~6.0 nT. These electrons would very shortly (<7 s) encounter a 5% larger (6.3 nT versus 6 nT) field strength downstream. Then electrons at 90°–103° PA (a fraction within the 90°–112°.5 PA bin) could presumably be reflected to 77°–90° PA, based on adiabatic invariance of $\sin^2\alpha/B$.

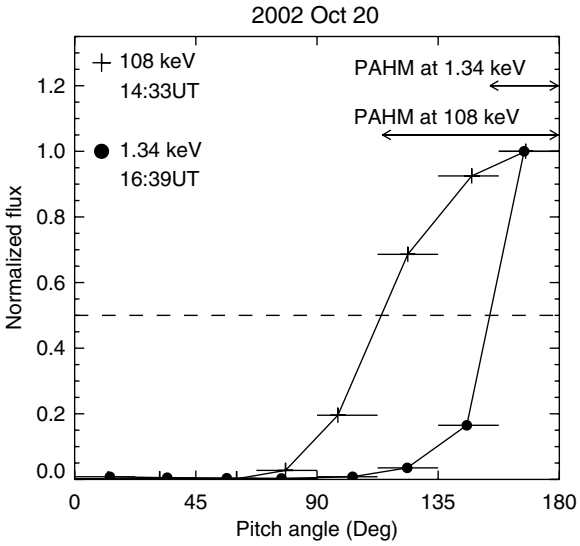

Figure 6. Background-subtracted electron PADs measured at 1.34 (dots) and 108 (crosses) keV for the 2002 October 20 event. The PADs are normalized to a maximum of 1. The PAHM is indicated by double-ended arrows at the top. Note that the inward-traveling flux is small but clearly evident at the 79° PA bin at 108 keV.

In EESA (below 30 keV), an inward-flux increase occurred in all inward PA bins during peak 1 (Figure 2, right). At each

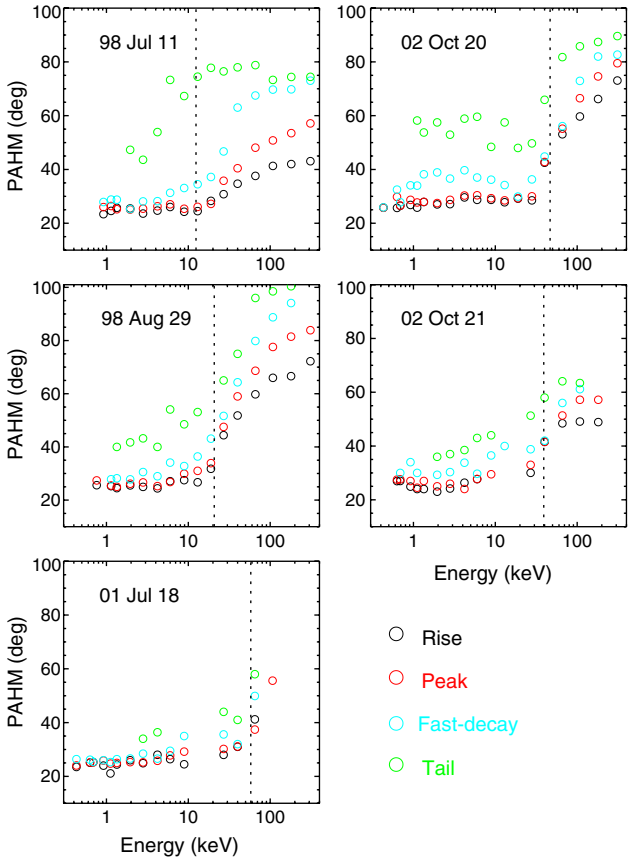

Figure 7. Energy dependence of the typical PAHM at the rise (black), peak (red), fast-decay (blue), and slow-tail (green) in the five solar impulsive electron events. In the 1998 July 11 and 2002 October 20 event, the tail PAHM is determined before the arrival of inward-traveling electrons in peak 2. The dash lines indicate the energy of electrons with $\rho_e = \rho_{Tp}$ (Table 1).

(A color version of this figure is available in the online journal.)

energy channel, this increase temporally correlated well with the flux increase in the field-aligned, outward PA bin but had a magnitude of only <2% of the outward flux. Such increase is likely caused by scattering of a small fraction of outward-traveling electrons at the entrance of EESA.

2.5. Summary of the 2002 October 20 Event

In the 2002 October 20 event, peak 1, detected at 0.3–310 keV, was the initial passage of outward-traveling electrons at the spacecraft. Some of these outward-traveling electrons were turned back at a radial distance of ∼1 AU (or a Parker spiral length of ∼1.7 AU) beyond the spacecraft by magnetic mirroring/scattering. Then they propagated inward and passed the spacecraft to produce peak 2 at energies of 27–180 keV. As those inward-traveling electrons continued propagating toward the Sun, they were eventually reflected back by converging IMF and then traveled outward again to yield peak 3 detected at 27–180 keV at 1 AU. At energies below 25 keV, peaks 2 and 3 might also be detected, but the count rate is poor.

During peak 1, the low-energy (∼0.4–27 keV) electrons exhibit strongly scatter-free temporal profiles and highly anisotropic PADs beamed along the IMF, indicating nearly scatter-free propagation through the IPM. The high-energy (∼30–300 keV) electrons exhibit strongly scatter-free temporal profiles but less anisotropic PADs that broaden with energy, indicating that high-energy electrons experienced some energy-dependent scattering and strong scattering occur near 1 AU.

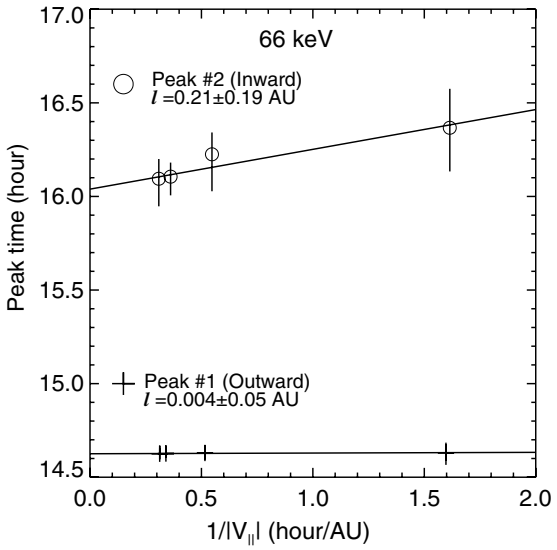

Figure 8. Examples of the PA dispersion analysis of the peak-flux time vs. inverse parallel speed at 66 keV for the 2002 October 20 event. The crosses indicate the times of peak 1 in four outward PA bins, and the circles indicate the times of peak 2 in four inward PA bins. The slope of the linear fit, $t(\alpha) = t_0' + l/V_\parallel(\alpha)$, gives an estimate of the travel distance l, if electrons propagate scatter-free. The α is determined as the average PA for each PA bin.

In addition, local inward-traveling populations were detected just across 90° PA at 66–310 keV during peak 1, likely resulting from local small-angle scattering or magnetic mirroring of outward-traveling electrons across 90° PA.

The velocity dispersion analysis of in situ peak times above 25 keV shows that the estimated injection peak times, t_{02} (1430 ± 0017UT) and t_{03} (1438 ± 0013UT) for peaks 2 and 3, respectively, appear systematically delayed relative to t_{01} (1412 ± 0002UT) for peak 1 (Figure 3, left). These estimates are obtained under the assumption that in a given peak, all the electrons above 25 keV traveled the same distance from the Sun to the spacecraft. However, if all the electrons in the three peaks were injected at the same t_{01} at the Sun, then the actual travel distance (the slope of the straight line connecting t_{01} and the in situ peak time) would be, for peak 2 (3), $L =$ ∼6.0, 6.2, 6.3, 6.4, and 6.7 AU (∼7.6, 8.2, 8.5, 8.5, and 9.1 AU), respectively, at 27, 40, 66, 108, and 180 keV. Thus, the delay of t_{02} and t_{03} implies that in peaks 2 and 3, electrons at higher energies traveled an actual longer distance than at lower energies. This is consistent with PAD observations above 25 keV, suggesting that higher energy electrons experienced relatively more scattering.

Four more events were analyzed—the 1998 July 11, 1998 August 29, 2001 July 18, and 2002 October 21 events—that have scatter-free time profiles and beamed PADs similar to the 2002 October 20 event. These are described in the Appendix and included in Figures 7 and 9 and Table 1.

3. SUMMARY AND DISCUSSION

We have investigated five solar impulsive electron events with strongly scatter-free temporal profiles at ∼0.3–300 keV (see Section 2 for the 2002 October 20 event and the Appendix for the other four events). Their electron PADs exhibit two different behaviors at low and high energies, with the energy transition E_0 varying from ∼10 to 40 keV from event to event (see Figure 7 and Table 1). At low energies (∼0.3 keV to E_0), the PAHM remains roughly constant below ∼25°–30° (corresponding to an actual PAHM of $\lesssim$15°) from onset through

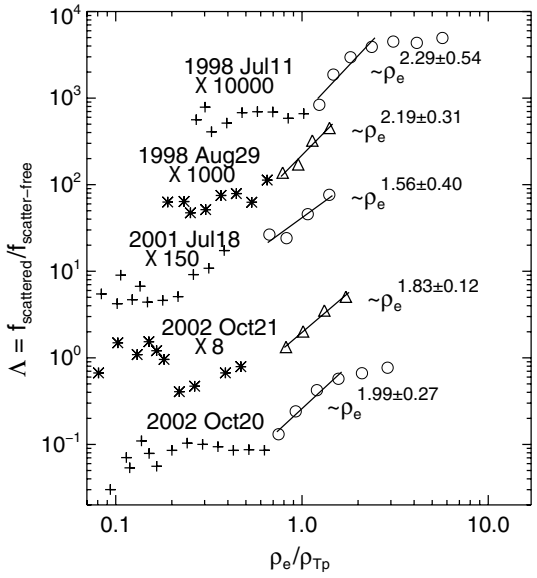

Figure 9. Ratio Λ of the peak flux of outward-traveling scattered electrons and field-aligned scatter-free electrons for the five solar impulsive electron events. The *X*-axis shows the electron gyroradius (ρ_e) in terms of the observed local thermal proton gyroradius (ρ_{Tp}) in the solar wind. For the 2002 October 20 event, the bottom crosses show the peak-flux ratio Λ for low-energy electrons that had essentially scatter-free PADs, and the bottom open circles show high-energy electrons that had scattered PADs. For the other four events, the open symbols (crosses or asterisks) show the ratio Λ at high (low) energies, which has been multiplied by different factors. The power-law fit to high-energy ratios is presented.

peak. At high energies (E_0 to 300 keV), the PAHM increases with both energy and time, e.g., from ∼30° (50°) at E_0 up to 85° (100°) at 300 keV at the peak (slow-tail). Thus, the high-energy electrons experienced more PA scattering, with scattering strength increasing with energy. The observed flux-time profiles, however, retain a rapid-rise, rapid-decay peak and the estimated path length is only ∼4%–18% longer than the smooth spiral field length, indicating that the scattering occurred near 1 AU. Simulations using the 1D telegraph equation (Lin 1974) indicate that strong scattering (mean free path $\lesssim$0.4 AU) in the inner solar system would produce a fast rise, but very slow decay (*e*-folding decay time of >4 hr).

In Figure 9, we plot Λ—the ratio of the peak flux of the scattered electrons (22.°5–90°, outward-traveling) to the peak flux of the unscattered electrons (outward-traveling, field-aligned, 0°–22.°5)—versus the electron gyroradius $\rho_e = \gamma m_e V_e/qB$, normalized by the local solar wind thermal proton gyroradius $\rho_{Tp} = \sqrt{2m_p kT_p}/qB$ (Boltzmann constant k), for the five electron events. kTp is obtained from the solar wind proton distribution measured by *WIND*/3DP ion electrostatic analyzer (PESA-L) for each event. For electrons with gyroradii less than ρ_{e0}, the peak flux ratio Λ is roughly constant at $\lesssim$0.1–0.15, while for electrons with gyroradii greater than ρ_{e0}, Λ increases with ρ_e from ∼0.1–0.15 to ∼0.5–0.8, roughly fitting to a power law with exponents of ∼1.6–2.3. The energy transition, E_0, always corresponds to a ρ_{e0} within a narrow range of 0.7–1.2 ρ_{Tp}, even though Tp varies by a factor of ∼5 (7–33 eV) and E_0 varies by a factor of 4 (10–40 keV) among the five electron events (Table 1). At the spatial scale of Tp, the solar wind turbulence power spectrum ($P \propto \lambda^{\beta}$) transitions from the inertial range ($\beta = 5/3$) above to the dissipation range ($\beta \sim 3$) below (Leamon et al. 1999). These results can be explained in terms of electron resonant interactions with the solar wind turbulence at $\lambda \sim \rho_e$. Low-energy electrons would be weakly scattered because of weak power densities for resonant fluctuations/waves at scale $\lambda < \rho_{Tp}$ (the dissipation range). High-energy electrons would scatter more due to higher power densities for fluctuations/waves at scale $\lambda > \rho_{Tp}$ (the inertial range), and the power-law increase of Λ with ρ_e may be associated with the power-law increase of turbulence power density with λ. Note that the 1998 July 11 event, detected during a magnetic cloud in the slow solar wind (indicated by the configuration of the observed IMF), gives similar results to the other four electron events detected in the normal fast solar wind, although the magnetic fluctuations are more transverse than in undisturbed solar wind (Leamon et al. 1998).

The proton temperature Tp decreases as $r^{-0.8}$ to $r^{-1.0}$ from 0.3 to 1.0 AU (Totten et al. 1995) and as $r^{-0.5}$ to $r^{-0.7}$ beyond 1 AU (Gazis & Lazarus 2003; Richardson et al. 1995), for both fast and slow solar wind, where r is the heliocentric distance. As solar energetic electrons at a given energy propagate away from the Sun, then, the resonant wave scale in terms of ρ_{Tp}, $\lambda/\rho_{Tp} \sim \rho_e/\rho_{Tp} \sim \gamma V_e/\sqrt{Tp}$, gradually increases with r. The heliocentric distance r_0 at which electrons would start to encounter efficient resonant scattering by waves of $\lambda \gtrsim \rho_{Tp}$ thus decreases with increasing electron energy, e.g., for 2, 20, and 100 keV electrons, r_0 is ∼9, 0.9, and 0.2 AU, respectively, assuming Tp varies as $r^{-1.0}$ with a value of 10 eV at 1 AU. En route to 1 AU, therefore, low-energy electrons would undergo very little scattering, while high-energy electrons experience efficient scattering along a distance $L = L(1AU) - L(r_0)$ that increases with energy. This is consistent with the PAD observations in the five events.

Cane & Erickson (2003) and Cane (2003) argued that the delays of ∼10–30 minutes in the injection at the Sun for high-energy electrons compared to type III bursts/low-energy electrons (Krucker et al. 1999; Haggerty & Roelof 2002; Wang et al. 2006) in most impulsive electron events are due to propagation effects in the IPM. We find evidence for scattering of high-energy electrons near 1 AU, but the estimated electron path length is only ∼1.3 AU, compared to a 1.1 AU length of a smooth spiral field length for a V_{SW} of ∼500 km s^{-1}. If the low-energy electrons travel scatter-free (i.e., 1.1 AU path length), and the extra path length for high-energy electrons is due to scattering, the travel time is only ∼2 minutes longer at 300 keV and ∼5 minutes longer at 30 keV, too short to explain the observed delays. This suggests that the injection at the Sun of the high-energy electrons is delayed.

We also find evidence for local small-angle scattering or magnetic mirroring across 90° PA for high-energy electrons. During the peak (No. 1) of outward-traveling electrons, inward-traveling electrons were detected just across 90° PA at 40–180 keV, 66–180 keV, and 66–300 keV, respectively, in the 1998 July 11, 1998 August 29, and 2002 October 20 events. Compared to electrons in the adjacent outward PA bin, these inward-traveling electrons show a slightly delayed maximum flux with an ∼7%–30% magnitude, suggesting that they were produced locally by small-angle scattering or magnetic mirroring of a fraction of the outward-traveling electrons in the adjacent PA bin across 90°. If the source is resonance scattering, then it cannot be explained by the theories where resonance scattering is suppressed around 90° PA (the so-called resonance gap; e.g., Jokipii 1966; Schlickeiser 1989). If the source is magnetic mirroring, then the downstream IMF strength would need to be larger by only <17%, since the $\gtrsim$ 17% stronger

magnetic field can reflect all the electrons, not just a fraction of them, in the 22.5 wide, outward PA bin next to 90° PA. In the three events, on the other hand, at energies below 40–66 keV, outward-traveling electrons mostly traveled along the magnetic field line and had relatively small fluxes in the PA bin next to 90° PA, so the produced local inward-traveling populations would be insignificant relative to the background.

In the 2002 October 20 event, a fraction of initial outward-traveling electrons (in peak 1) were turned back likely by structures with enhanced IMF/waves at the heliocentric distance of ~2 AU (Figure 3). These structures might be the corotating interaction region generated by the compression between fast and slow solar wind, with shocks forming typically at a heliocentric distance of >1.5 AU (Smith & Wolfe 1976). As these electrons traveled toward the Sun, they were mirrored back by converging IMF and propagated outward again. These inward-traveling and newly outward-traveling populations were successively detected above 25 keV at 1 AU, each showing a roughly symmetric peak (Nos. 2 and 3, respectively) in the flux-time profile but rather isotropic PADs. Such observations may result from the combination of scattering and adiabatic magnetic focusing/broadening during propagation. The velocity dispersion analysis (Figure 3) suggests that at higher energies, the scattering was relatively stronger and then led to an actual longer electron path. In the 1998 July 11 event, similar electron populations, peaks 2 and 3, were also detected, and they were likely due to reflection during propagation along the closed IMF lines in the magnetic cloud.

We thank Davin Larson, Gang Li, and Stuart Bale for helpful discussions, and the MFI team on *WIND* for sharing data with us. This research at Berkeley is supported in part by NASA grant NNX08AE34G. R. Lin was also supported in part by the WCU grant (No. R31-10016) funded by the Korean Ministry of Education, Science and Technology.

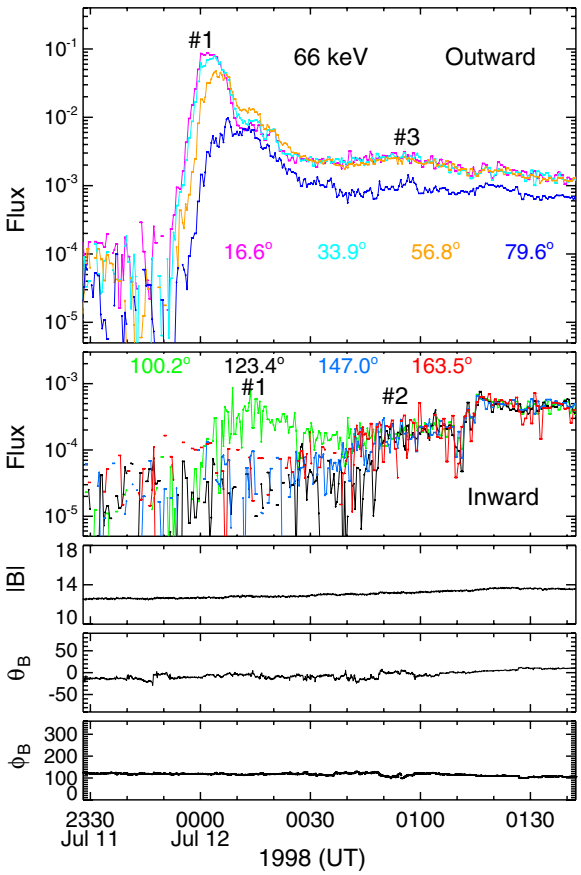

Figure A1. Temporal profiles of background-subtracted electron fluxes at 66 keV in four outward-traveling and four inward-traveling PA bins for the 1998 July 11 event. Colored curves indicate the flux in different PA bins. The bottom panels show the magnitude, polar angle, and azimuthal angle of the IMF. (A color version of this figure is available in the online journal.)

APPENDIX

THE OTHER FOUR IMPULSIVE ELECTRON EVENTS

A.1. The 1998 July 11 Event

The 1998 July 11 event was detected near the center of a magnetic cloud where the IMF line is presumably less coiled (the topology of magnetic flux rope favors more helical field lines at larger distance from its axis; Larson et al. 1997). In this event, the IMF pointed away from the Sun. Figure A1 shows background-subtracted electron fluxes versus time in four outward and four inward PA bins at 66 keV. The flux-time profiles exhibit three peaks, 1 at ~0002UT, 2 at ~0055UT, and 3 at ~0057UT, on July 12. An abrupt flux "bump"occurred during 0009UT–0021UT simultaneously in all outward PA bins at all energies from 27 to 310 keV, and another abrupt flux increase occurred at 0110UT simultaneously in all inward PA bins (also evident in outward PA bins that have low fluxes) at all energies from 27 to 108 keV, both probably caused by the passage of a flux tube/channel of high particle fluxes at those energies (e.g., Mazur et al. 2000; Anderson & Dougherty 1986).

Peak 1, detected at ~0.9–310 keV, was caused by the initial passage of outward-traveling electrons at the spacecraft. The velocity dispersion of the peak times above 25 keV gives an injection peak time of 2340 ± 0002UT and a path length of 1.21 ± 0.10 AU, comparable to the 1.16 AU smooth spiral field length calculated for the measured average V_{SW} of ~390 km s^{-1}. Because of closed connected IMF lines within the magnetic cloud (unlike open IMF lines in the undisturbed solar wind), sooner or later, electrons in peak 1 propagated toward the Sun and some of them were mirrored back by stronger field. At 1 AU, the mirrored electrons started to arrive about 20–40 minutes after peak 1 and they produced a peak (No. 2) at 27–180 keV in inward PA bins (see Figure A1, for example). But their velocity dispersion was obscured by an abrupt flux increase at ~0110UT. As these electrons continued propagating along closed IMF lines, they were mirrored back again by strong IMF close to the Sun. Then they passed the spacecraft once more to yield a small peak (No. 3) at 27–180 keV in outward PA bins, superimposed on the slow-decay tail of peak 1. The velocity dispersion analysis of those peak times gives an injection peak time of 2343 ± 0020UT and a path length of 3.56 ± 0.81 AU.

During peak 1, the PADs of these outward-traveling electrons can be divided into two groups (the top left panel of Figure 7). At 0.9–13 keV, the PAHM is below ~27° (limited by the instrumental resolution) and does not change from onset through peak; afterward, it increases with time until reaches ~50°–70° in the decay. At ~19–300 keV, the PADs become broader and their PAHM increases with both energy and time, e.g., from ~30° (~43°) at onset to ~47° (~73°) at the fast decay for 27 keV (310 keV). These suggest that low-energy electrons propagated nearly scatter-free, while high-energy electrons experienced more scattering with scattering strength increasing with energy. In addition, for peak 1, the PA dispersion analysis of peak times

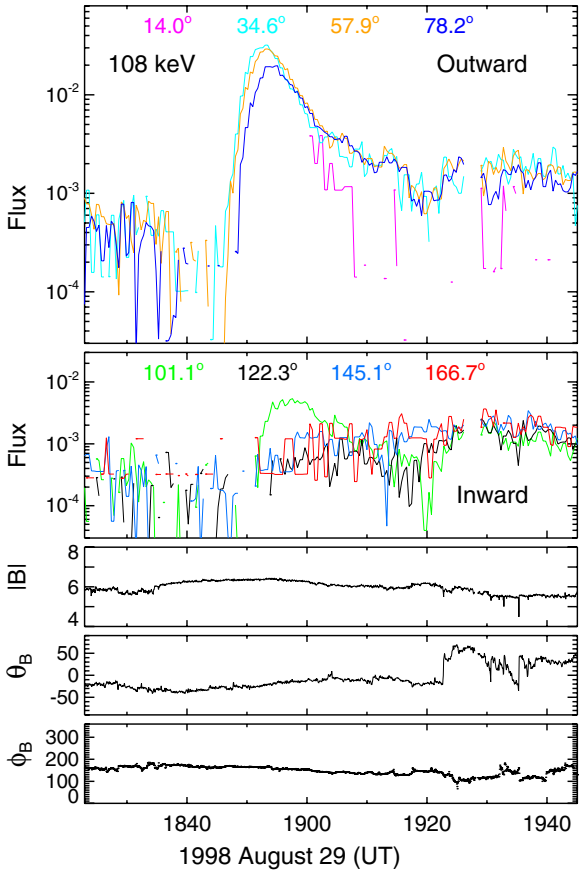

Figure A2. Temporal profiles of background-subtracted electron fluxes at 108 keV in four outward-traveling and four inward-traveling PA bins for the 1998 August 29 event. Colored curves indicate the flux in different PA bins. The bottom panels show the magnitude, polar angle, and azimuthal angle of the IMF.

(A color version of this figure is available in the online journal.)

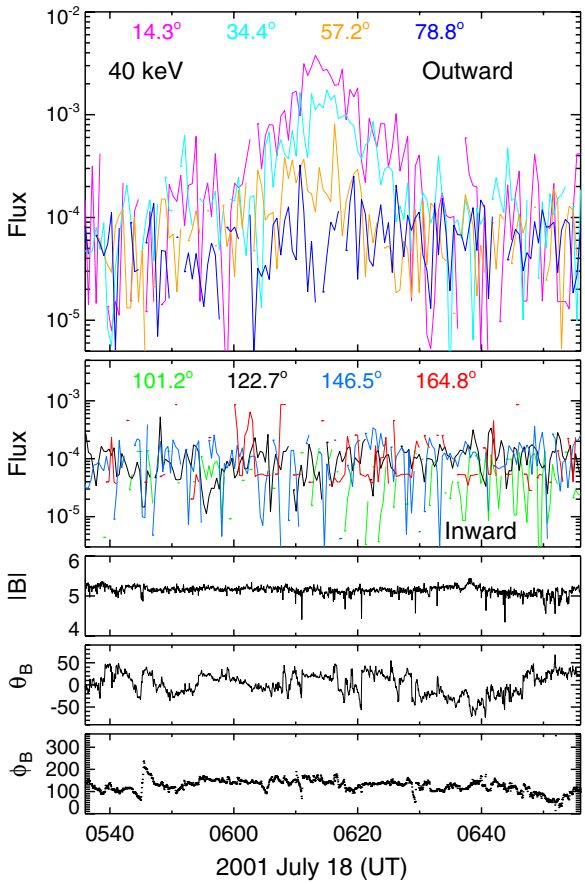

Figure A3. Temporal profiles of background-subtracted electron fluxes at 40 keV in four outward-traveling and four inward-traveling PA bins for the 2001 July 18 event. Colored curves indicate the flux in different PA bins. The bottom panels show the magnitude, polar angle, and azimuthal angle of the IMF.

(A color version of this figure is available in the online journal.)

in different PA bins gives, on average, a travel distance l of 0.09 ± 0.03 AU and 0.28 ± 0.14 AU, respectively, at energies above 15 keV and below, indicative of stronger local scattering for high-energy electrons.

During peak 1, the local inward-traveling electrons were clearly detected at 40–180 keV only in the 100° PA bin, with a flux maximum slightly delayed from the adjacent outward 80° PA bin (see Figure A1, for example). The flux ratio of the inward 100° PA bin to the outward 80° PA bin is 7%–10% at the peak and increases to 20%–30% afterward. The observed inward flux was due to inward-traveling electrons likely resulting from local small-angle scattering or mirroring across 90° PA.

A.2. The 1998 August 29 Event

The 1998 August 29 event was detected at ∼0.8–300 keV with the IMF pointing away from the Sun and the average V_{SW} of ∼550 km s^{-1} (corresponding to a 1.09 AU smooth spiral field length). A 1.14 ± 0.10 AU path length is obtained from the velocity dispersion analysis of peak times above 25 keV. Figure A2 shows background-subtracted electron fluxes versus time in four outward and four inward PA bins at 108 keV. The flux-time profiles of outward-traveling electrons exhibit a rapid-rise, rapid-decay peak, followed by a slow decay at much lower flux levels. A data gap occurred from ∼1813UT to 1900UT in the field-aligned (0°–22.5) PA bin at all energies above 25 keV. In this event, electron PADs exhibit different behaviors at energies below ∼10 keV and above (the middle left panel of Figure 7). At ∼0.8–10 keV, the PAHM remains below ∼27° (limited by the instrumental resolution) through the peak. At ∼13–300 keV, the PAHM increases with both energy and time from ∼27° at onset for 13 keV up to ∼100° in the slow tail for 200–300 keV.

During the peak, the local inward-traveling electrons were detected at 66–180 keV only in the 101° PA bin, with a flux maximum delayed from the adjacent outward 78° PA bin (see Figure A2, for example). The flux ratio of the inward 101° PA bin to the outward 78° PA bin is ∼20%–30% at the peak and afterward increases to 40%–60%, indicating that these inward-traveling electrons originated from local small-angle scattering or mirroring of a fraction of electrons in the 78° PA bin across 90° PA.

A.3. The 2001 July 18 Event

The 2001 July 18 event was detected at ∼0.4–180 keV with the V_{SW} of 670 km s^{-1} (corresponding to a 1.06 AU smooth spiral field length) and the IMF pointing away from the Sun. The velocity dispersion analysis of peak times above 25 keV gives a path length of 1.13 ± 0.35 AU. In this electron event, the PAHM of PADs remains roughly constant below ∼25° (limited by the instrumental resolution) from onset through peak at energies below ∼10 keV, and it broadens with both energy and time at energies above 40 keV from ∼30° up to ∼60° (bottom left

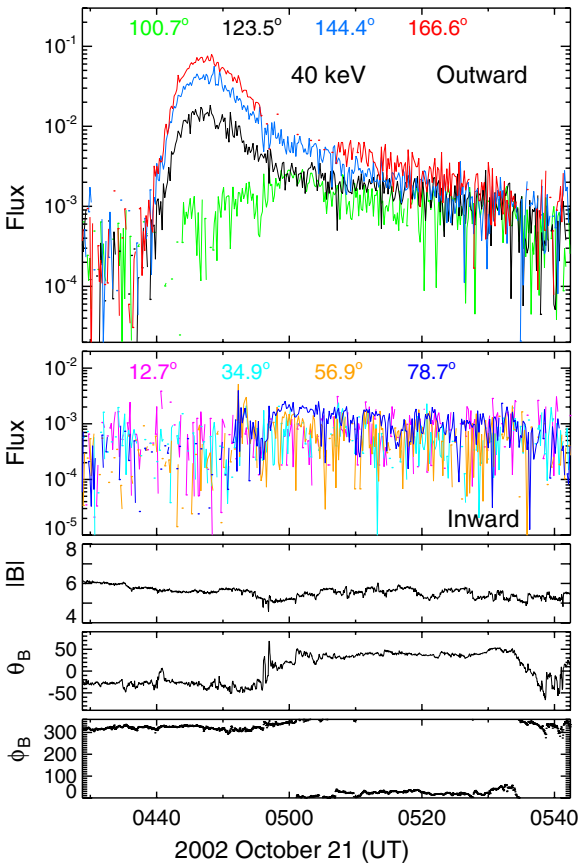

Figure A4. Temporal profiles of background-subtracted electron fluxes at 40 keV in four outward-traveling and four inward-traveling PA bins for the 2002 October 21 event. Colored curves indicate the flux in different PA bins. The bottom panels show the magnitude, polar angle, and azimuthal angle of the IMF.

(A color version of this figure is available in the online journal.)

panel of Figure 7), while count statistics was poor between 10 and 30 keV. Figure A3 shows background-subtracted electron fluxes versus time in four outward and four inward PA bins at 40 keV.

A.4. The 2002 October 21 Event

The 2002 October 21 event was detected at ∼0.3–180 keV with the IMF pointing toward the Sun. The velocity dispersion of peak times above 25 keV gives a 1.14 ± 0.10 AU path length, close to the 1.07 AU smooth spiral field length calculated for the observed V_{SW} of 610 km s^{-1}. In this event, the PAHM remains below ∼28° (limited by the instrumental resolution) from onset through peak at energies below ∼10 keV, and it broadens with both energy and time above 25 keV from ∼30° up to ∼65° (the middle right panel of Figure 7), while poor statistics occurred between 10 and 25 keV. Figure A4 shows background-subtracted electron fluxes versus time in four outward and four inward PA bins at 40 keV.

REFERENCES

Anderson, K. A., & Dougherty, W. M. 1986, Sol. Phys., 103, 165
Anderson, K. A., & Lin, R. P. 1966, Phys. Rev. Lett., 16, 1121
Berger, M. J., Seltzer, S. M., Chappell, S. E., Humphreys, J. C., & Motz, J. W. 1969, Nucl. Instrum. Methods, 69, 181
Cane, H. V. 2003, ApJ, 598, 1403
Cane, H. V., & Erickson, W. C. 2003, J. Geophys. Res., 108, 1203
de Koning, C. A., Gosling, J. T., Skoug, R. M., & Steinberg, J. T. 2006, J. Geophys. Res., 111, A04101
de Koning, C. A., Gosling, J. T., Skoug, R. M., & Steinberg, J. T. 2007, J. Geophys. Res., 112, A04101
Ergun, R. E., et al. 1998, ApJ, 503, 435
Forbush, S. E. 1946, Phys. Rev., 70, 771
Gazis, P. R., & Lazarus, A. J. 2003, Geophys. Res. Lett., 9, 431
Gosling, J. T., Skoug, R. M., & McComas, D. J. 2003, Geophys. Res. Lett., 30, 1697
Haggerty, D. K., & Roelof, E. C. 2002, ApJ, 579, 841
Jokipii, J. R. 1966, ApJ, 145, 616
Krucker, S., Larson, D. E., Lin, R. P., & Thompson, B. J. 1999, ApJ, 519, 864
Larson, D. E., et al. 1997, Geophys. Res. Lett., 24, 1911
Leamon, R. J., Smith, C. W., & Ness, N. F. 1998, Geophys. Res. Lett., 25, 2505
Leamon, R. J., Smith, C. W., Ness, N. F., & Wong, H. K. 1999, J. Geophys. Res., 104, 22331
Lepping, R. P., et al. 1995, Space Sci. Rev., 71, 207
Lin, R. P. 1974, Space Sci. Rev., 16, 189
Lin, R. P. 1985, Sol. Phys., 100, 537
Lin, R. P., Potter, D. W., Gurnett, D. A., & Scarf, F. L. 1981, ApJ, 251, 364
Lin, R. P., et al. 1995, Space Sci. Rev., 71, 125
Mazur, J. E., Mason, G. M., Dwyer, J. R., Giacalone, J., Jokipii, J. R., & Stone, E. C. 2000, ApJ, 532, L79
Potter, D. W., Lin, R. P., & Anderson, K. A. 1980, ApJ, 236, L97
Reames, D. V. 1995, Rev. Geophys., 33, 585
Reames, D. V. 1999, Space Sci. Rev., 90, 413
Richardson, J. E., Paularena, K. I., Lazarus, A. J., & Belcher, J. W. 1995, Geophys. Res. Lett., 22, 325
Schlickeiser, R. 1989, ApJ, 336, 243
Smith, E. J., & Wolfe, J. H. 1976, Geophys. Res. Lett., 3, 137
Totten, T. L., Freeman, J. W., & Arya, S. 1995, J. Geophys. Res., 100, 13
Van Allen, J. A., & Krimings, S. M. 1965, J. Geophys. Res., 70, 5737
Wang, L., Lin, R. P., Krucker, S., & Gosling, J. T. 2006, Geophys. Res. Lett., 33, L03106